PHYSICAL REVIEW D VOLUME 39, NUMBER 8 15 APRIL 1989

Nonlinear solutions for initial data in the vacuum Einstein equations in plane symmetry

Peter Anninos and Joan Centrella
Department of Physics and Atmospheric Science, Drexel University, Philadelphia, Pennsylvania 19104

Richard Matzner
Department of Physics and Center for Relativity, The University of Texas at Austin, Austin, Texas 78712

(Received 29 August 1988)

We present a study of the parameter space of solutions for initial data in the plane-symmetric vacuum Einstein equations. We use the York splitting into free and constrainted variables to find analytic solutions to the momentum and Hamiltonian constraints to first and second perturbative orders. We construct a numerical code to solve the equations in the full nonperturbative regime and present extensive tests to verify its accuracy. We parametrize the solution space by the amplitude of waves in the free data and present examples in several cases of interest. These results clearly show the differences among solutions to the linear, weakly nonlinear (second-order), and fully nonlinear equations.

I. INTRODUCTION

The aim of this work is to understand the basic nonlinear physics of the gravitational field as exemplified by solutions to the classical Einstein vacuum field equations. For all the progress in recent years in solutions to these equations in complex multidimensional systems, e.g., the collision of two black holes[1,2] and axisymmetric stellar collapse,[3,4] many basic issues remain unresolved. For example, what is the nature of the basic nonlinear gravitational self-interaction? Do traveling waves steepen to form shocks or spread out through dispersion? What is the physical basis for the so-called gravitational "soliton" solutions?[5-10] These general-relativistic problems are necessarily complicated by the possibility of dynamical coordinate systems and their entanglement with the physical gravitational degrees of freedom. Nevertheless, the answers to questions such as these, posed in the contexts of other continuum field theories such as electrodynamics and hydrodynamics, have greatly increased our understanding of the physical basis of these theories and have allowed us to tackle more complicated situations.

We begin studying the simplified problem of one-dimensional (1D), i.e., one spatial dimension plus time, plane-symmetric solutions. This includes the evolution of standing waves, as well as the propagation and interaction of traveling waves. Of course, questions regarding the generality of such results, in particular their sensitivity to dimensionality (different physical behavior in one, two, or three dimensions), must be kept in mind. Nonetheless, such simple systems often form the building blocks for more complex multidimensional problems. For example, the evolution of 2D axisymmetric hydrodynamic jets is resplendent with shocks and rarefactions first elucidated in 1D (Ref. 11).

Our approach uses a synergistic combination of analytic and numerical techniques.[12,13] On the one hand, we carry out a perturbation treatment of the equations to second order. Thus, we have an analytic description of the behavior of the field theory in both the linearized limit and the weakly nonlinear second-order regime. In addition, we construct a numerical code to solve for fully developed nonlinear solutions. These two techniques complement one another. For example, unlike the case of the linearized limit, there is no guarantee that our system has a valid second-order description; it could undergo an abrupt change in behavior when terms beyond first order reach a certain level. However, a numerical solution can be used as a scout for the onset of nonlinearity and, in particular, the existence of a second-order regime. In fact, it was just such a numerical investigation at an earlier stage of this work[14] that led to the present study. In return, the perturbative solutions can serve as test-bed calculations for verifying the accuracy of the numerical code. Such interaction between analytic and numerical techniques is critical to the success of this work.

In this paper we concentrate on the initial-value problem for plane-symmetric solutions to the vacuum Einstein equations. We work within the context of the "3+1" splitting of spacetime[15] and use the formalism developed by York[16] to decompose the initial data into its freely specifiable and constrained parts. The resulting equations are the Hamiltonian constraint, which is nonlinear in the conformal factor for which we solve, and the momentum constraint, which is linear in the momentum variables but nonlinear in the freely specifiable data.

We find analytic solutions to these equations to first and second order. In addition, we obtain analytic solutions to the momentum constraint to all orders in certain cases, although this is not possible for the Hamiltonian constraint in these cases due to its intrinsic nonlinearity. We construct a numerical code and demonstrate that it agrees with the analytic solutions in their region of validity. Special effort is made to develop a means of testing the numerical solution of the nonlinear Hamiltonian constraint. The code is then used to solve the initial-value problem in the fully developed nonlinear regime.

Our methodology is to study the solution space of the initial-value problem as a function of parameters in the freely specifiable data. Several examples are given showing the responses of the system to increasing the amplitude and changing the wavelengths in the free data. These examples help clarify which parameters, or combinations of parameters, are important in determining the nonlinear behavior.

II. SYSTEM VARIABLES AND BASIC EQUATIONS

The 1D spacetime metric we treat is

$$ds^2=-(\alpha^2-A^2\beta^2)dt^2+2A^2\beta dz\,dt + A^2(dx^2+h^2dy^2+dz^2)\ , \tag{2.1}$$

where α, β, A, and h are functions of z and t. The metric variable h describes transverse anisotropy of the solution. The lapse function α and the shift vector β determine the evolution of the coordinate system off the initial spacelike slice. Since we consider only the initial-value problem in this paper, α and β will not enter our analysis. The system we consider is assumed to be periodically identified in the spatial coordinate z. Thus, all variables must be periodic with period equal to the identification length L.

This metric is well suited to the study of plane gravitational waves. As a solution to the vacuum Einstein equations, it produces spacetimes which belong to the Gowdy T^3 family of models,[17,18] although in a very different gauge. Using the form (2.1), a numerical code has been built[19,20] and used to solve problems in cosmic nucleosynthesis,[21] inflationary cosmology,[22] and the evolution of nonlinear gravitational waves.[14] In this study we take a somewhat different approach, using the York[16] formalism to decompose the metric and momentum variables into their freely specifiable and constrained pieces. As we shall demonstrate, this provides an excellent framework for carrying out parameter-space studies of the solutions to the equations. In this paper we consider only the initial-value problem in vacuum; the evolution equations and the extension of this work to the case of sources will be presented in later papers.

In the "3+1" split, the initial-value equations in vacuum become the Hamiltonian constraint

$$R+(\mathrm{tr}K)^2-K_{ij}K^{ij}=0 \tag{2.2}$$

and the momentum constraint

$$D_j(K^{ij}-\gamma^{ij}\mathrm{tr}K)=0\ . \tag{2.3}$$

Here, γ_{ij} is the three-metric of the spacelike slice, K_{ij} is the extrinsic curvature, and $\mathrm{tr}K\equiv\gamma^{ij}K_{ij}$ is its trace. Lower case Latin letters denote spatial indices: $i,j=1,2,3$. D_j is the covariant derivative in the slice and R is the Ricci scalar formed from the three-metric. See York[16] for further details. The Hamiltonian constraint amounts to taking into proper account the gravitational energy density associated with the nonlinearity of the Einstein field. The momentum constraint can be interpreted as guaranteeing that there is no net momentum. Notice that when $h=1$, our three-space is a flat, isotropically expanding three-torus. Thus $h-1$ can be considered the perturbation away from this solution. The momentum constraint (2.3) is automatically satisfied when $h-1=0$; at first order it sets a total derivative to zero. It becomes interesting only at second perturbation order. The condition it imposes is identical to the requirements of linearization stability.[23,24] For these perturbations from a flat torus, the condition arises simply as a requirement of periodicity. Our system, even in the full nonlinear regime, must satisfy this periodicity requirement, which is thus the nonlinear manifestation of linearization stability. This will become more apparent as we proceed.

The York procedure for solving the constraint equations (2.2) and (2.3) begins by defining a conformal three-metric $\hat{\gamma}_{ij}$,

$$\gamma_{ij}=\varphi^4\hat{\gamma}_{ij}\ , \tag{2.4}$$

where φ is called the conformal factor. Quantities with a circumflex (^) are conformally transformed. Next, form the trace-free part of the extrinsic curvature

$$A_{ij}=K_{ij}-\tfrac{1}{3}\gamma_{ij}\mathrm{tr}K\ , \tag{2.5}$$

and define its conformal transformation

$$\hat{A}^{ij}=\phi^{10}A^{ij}\ . \tag{2.6}$$

We will treat $\mathrm{tr}K$ as a conformal invariant, $\widehat{\mathrm{tr}}\hat{K}=\hat{\gamma}^{ij}\hat{K}_{ij}\equiv\mathrm{tr}K$. The tensor $\hat{A}_{ij}$ is then split so that

$$\hat{A}^{ij}=\hat{A}_*^{ij}+(\hat{l}w)^{ij}\ , \tag{2.7}$$

where $\hat{A}_*^{ij}$ is the transverse-traceless part, and $\hat{l}w$ is a tensor formed from a vector potential $\mathbf{w}$ and is the longitudinal part of $\hat{A}_{ij}$. For the particular case of vacuum, and assuming that our models have no $\hat{z}$ Killing vectors, i.e., that they are really inhomogeneous in the z direction, then $\mathbf{w}=0$ (Ref. 3).

The conformally transformed Hamiltonian constraint is then

$$\hat{\Delta}\varphi=\tfrac{1}{8}\varphi[\hat{R}-\hat{A}_{ij}\hat{A}^{ij}\varphi^{-8}+\tfrac{2}{3}\varphi^4(\mathrm{tr}K)^2]\ , \tag{2.8}$$

where $\hat{\Delta}=\hat{\gamma}^{ij}\hat{D}_i\hat{D}_j$. The momentum constraint splits into two conditions on $\hat{A}_*^{ij}$:

$$\hat{D}_j\hat{A}_*^{ij}=0 \tag{2.9a}$$

with

$$\widehat{\mathrm{tr}}\hat{A}_*=\hat{\gamma}^{ij}\hat{A}_{*ij}=0\ , \tag{2.9b}$$

which must hold since $\hat{A}_*^{ij}$ is transverse and traceless. In addition, there is an equation for the vector potential $\mathbf{w}$ which has the trivial solution $\mathbf{w}=0$ for the vacuum case discussed here.

York's prescription for setting the initial data is as follows. First, specify the free data $\hat{\gamma}_{ij}$, $\mathrm{tr}K$, and $\hat{A}_*^{ij}$ [subject to the conditions (2.9)]. Then, solve the Hamiltonian constraint (2.8) for φ and, in the general nonvacuum case, an equation for **w**. Finally, recompose the data using Eqs. (2.4) and (2.5) to obtain a set (γ_{ij}, K_{ij}) that satisfy the full (untransformed) constraint equations (2.2) and (2.3).

In our case, the conformal metric is

$$\hat{\gamma}_{ij} = \mathrm{diag}(1, h^2, 1) , \tag{2.10}$$

and $\varphi^4 = A^2$. We require that K_{ij} be diagonal; by Eqs. (2.5)–(2.7), A_{ij}, $\hat{A}_{ij}$, and $\hat{A}_{*ij}$ are also diagonal. This means that there is one free component of A_{ij} which we take to be

$$\eta = A^x_x - A^y_y . \tag{2.11}$$

The conformal ($\hat{\ }$) and starred ($*$) versions of this transverse-momentum variable are similarly defined, viz.,

$$\hat{\eta} = \hat{A}^{\,x}_{\,x} - \hat{A}^{\,y}_{\,y} \tag{2.12}$$

and

$$\hat{\eta}_* = \hat{A}^{\,x}_{\,*x} - \hat{A}^{\,y}_{\,*y} . \tag{2.13}$$

Note that in this vacuum case $\hat{\eta}_*$ and $\hat{A}^{\,ij} = \hat{A}^{\,ij}_{\,*}$. The momentum constraint then is simply the expression of the demand that $\hat{A}^{\,i}_{\,*j}$ be transverse:

$$\hat{A}^{\,z\prime}_{\,*z} + \frac{3}{2}\frac{h'}{h}\hat{A}^{\,z}_{\,*z} + \frac{1}{2}\frac{h'}{h}\hat{\eta}_* = 0 \tag{2.14a}$$

or

$$(\hat{A}^{\,z}_{\,*z} h^{3/2})' = -\tfrac{1}{2} h^{1/2} h' \hat{\eta}_* . \tag{2.14b}$$

Here, prime (′) means $\partial/\partial z$. The Hamiltonian constraint is

$$h^{-1}(\phi' h)' = \tfrac{1}{8}\phi \left[-2\frac{h''}{h} + \tfrac{2}{3}(\mathrm{tr}K)^2 \phi^4 - [\tfrac{1}{2}\hat{\eta}^2 + \tfrac{3}{2}(\hat{A}^{\,z}_{\,z})^2]\phi^{-8} \right] . \tag{2.15}$$

Our strategy for solving these initial-value equations is as follows. We consider h, $\hat{\eta}_*$, and tr$K$ to be freely specifiable. In particular, we work exclusively with spacelike slices having tr$K = (\mathrm{tr}K)(t)$ only, the constant mean curvature slices. Equations (2.14) and (2.15) are then solved for the rest of the data. Suitable parametrization of and choices for h and $\hat{\eta}_*$ allows us to explore the solution space of the initial-value problem.

III. PERTURBATION EXPANSION

We now carry out a perturbation solution of the initial value Eqs. (2.14) and (2.15) to second order. By second order, we mean that we take some analytically known "background" solution and consider perturbations to second order in some smallness parameter.

The solutions from which we choose to perturb are the spatially homogeneous Kasner[25] solutions to the vacuum field equations. They are usually expressed in terms of proper time T as

$$ds^2 = -dT^2 + T^{2p_1}dx^2 + T^{2p_2}dy^2 + T^{2p_3}dz^2 , \tag{3.1}$$

where the Einstein equations restrict the constant parameters p_1, p_2, and p_3:

$$p_1 + p_2 + p_3 = 1 , \tag{3.2}$$

$$p_1^2 + p_2^2 + p_3^2 = 1 . \tag{3.3}$$

These solutions fit our metric form (2.1) with the choices $\alpha = 1$ and $\beta = 0$, plus the restriction that $p_1 = p_3$. There are two such axisymmetric Kasner models:

case (C): $p_1 = \frac{2}{3}$, $p_2 = -\frac{1}{3}$

(axisymmetric vacuum expanding cosmology) (3.4a)

and

case (F): $p_1 = 0$, $p_2 = 1$

(flat space in expanding Milne-type coordinates) . (3.4b)

Note that the full 1D problem, such as our perturbed metric, involves functions of time and the spatial coordinate z, but that the z direction is *not* the symmetry axis of our background solutions. Thus gravitational waves propagating in the z direction can be considered.

The analysis here will consider perturbations from each of these solutions (3.4). The York variables to be perturbed in each case are

case (C)	case (F)	
$\phi = t^{1/3}(1 + \phi_1 + \phi_2)$	$\phi = 1 + \phi_1 + \phi_2$	(3.5)
$h = t^{-1}(1 + h_1 + h_2)$	$h = t(1 + h_1 + h_2)$	(3.6)
$\mathrm{tr}K = -t^{-1}$	$\mathrm{tr}K = -t^{-1}$	(3.7)
$\hat{A} = -\frac{1}{3}t(1 + \hat{A}_1 + \hat{A}_2)$	$\hat{A} = \frac{1}{3}t^{-1}(1 + \hat{A}_1 + \hat{A}_2)$	(3.8)
$\hat{\eta} = -t(1 + \hat{\eta}_1 + \hat{\eta}_2)$	$\hat{\eta} = t^{-1}(1 + \hat{\eta}_1 + \hat{\eta}_2)$	(3.9)

where $\hat{A} \equiv \hat{A}^{\,z}_{\,z} = \hat{A}^{\,z}_{\,*z}$ and $\hat{\eta} \equiv \hat{\eta}_*$. The meaning of this perturbation expansion is that quantities with a subscript 1 are first order in some smallness parameter ϵ, while quantities with a subscript 2 are second order. Note that we have chosen not to perturb tr$K$; this means that the initial spacelike slice in both the background and spacetimes have the same mean curvature.

In these variables, the Hamiltonian constraint (2.15) to first order becomes

$$\phi_1'' = -\tfrac{1}{4}h_1'' + f(t)(\phi_1 - \tfrac{1}{8}\hat{\eta}_1 - \tfrac{1}{24}\hat{A}_1) , \tag{3.10}$$

where $f(t) = t^{-2/3}$ [case (C)], $f(t) = t^{-2}$ [case (F)]. The different explicit powers of t for case (C) and case (F) arise from the different explicit powers of t in Eqs. (3.5)–(3.9). The momentum constraint at first order reads, in both cases,

$$\hat{A}_1' + 3h_1' = 0 . \tag{3.11}$$

In these equations, $\hat{\eta}_1$ and h_1 are considered free variables, given the restriction of periodicity in the spatial direction. Because of the periodicity requirement we take

$$h_1=\sum h_{1(m)}\sin(2\pi mz/L+\delta_{1(m)}) \tag{3.12}$$

and

$$\hat{\eta}_1=\sum \hat{\eta}_{1(m)}\sin(2\pi mz/L+\delta_{1(m)}) \ . \tag{3.13}$$

The phase $\delta_{1(m)}$ must be the same function of (m) for both h_1 and $\hat{\eta}_1$ [cf. Eq. (3.18) below]. We take the solution

$$\hat{A}_1=-3h_1 \tag{3.14}$$

to the momentum constraint (3.11); this sets the integration constant to zero as discussed below. Then we substitute Eq. (3.14) into Eq. (3.10) and use Eqs. (3.12) and (3.13) to find

$$\begin{aligned}\phi_1=\sum_n &\left[\left[\frac{2\pi n}{L}\right]^2+f(t)\right]^{-1}\\ &\times\left\{\tfrac{1}{8}f(t)\hat{\eta}_{1(n)}-\left[\frac{1}{4}\left[\frac{2\pi n}{L}\right]^2+\tfrac{1}{8}f(t)\right]h_{1(n)}\right\}\\ &\times\sin\left[\frac{2\pi nz}{L}+\delta_{1(n)}\right] .\end{aligned} \tag{3.15}$$

To *second* order, the momentum constraint reads

$$\hat{A}'_2+3h'_2=3h_1h'_1-\tfrac{3}{2}\hat{A}_1h'_1-\tfrac{3}{2}h'_1\hat{\eta}_1 \ . \tag{3.16}$$

At this level the requirement of periodicity becomes significant. For periodicity, we have of course

$$\oint dz\, F'(z)=0 \tag{3.17}$$

for arbitrary F where the notation $\oint dz$ means integration $\int_0^L dz$, i.e., integration over the identification length L. Use the solution (3.14) to the linearized momentum constraint to express $\hat{A}_1$ in terms of h_1. With this substitution, all the terms in Eq. (3.16) can be immediately expressed as perfect differentials except the one involving $h'_1\hat{\eta}_1$. Periodicity, however, demands that the first-order solutions obey

$$\oint h'_1\hat{\eta}_1 dz=0 \ . \tag{3.18}$$

Thus, h_1 and $\hat{\eta}_1$ must be such that $h'_1\hat{\eta}_1$ is a perfect differential, and this must hold for each wave number. Using the forms (3.12) and (3.13), we see that h_1 and $\hat{\eta}_1$ must have mode terms that are *in phase in z* for each mode number, a result which was anticipated to simplify the first-order solution above. This result, that a certain second-order combination of first-order perturbations vanish when periodicity is considered, is the promised manifestation of linearization stability in this problem.

Brill[24] has given a particularly clear discussion of the question of linearization stability. Essentially, linearization *instability,* meaning potential difficulty in extending solutions to the linearized equations to solutions to the full equations, arises only when the background solution possesses Killing vectors, i.e., symmetry. The conditions arise from the Hamiltonian constraint if there is a timelike Killing vector, which is not the case for our cosmological models (the *flat* space in expanding coordinates of course does have a timelike Killing vector, but we explicitly demonstrate below that, in this gauge and for perturbations of the form we consider, there are no additional restrictions arising from the second-order Hamiltonian constraint), and from the momentum constraint contracted into the Killing vector for spacelike Killing vectors. Here we have only spatial Killing vectors ∂_x,∂_y, and the background Killing vector ∂_z. In fact, our functions depend only on z. Brill obtains the lowest-order (i.e., the second-order) constraint arising from the linearization stability requirement:

$$\int [\mathcal{L}_K(\delta g_{ij}^{TT})](\delta\pi^{ijTT})d^3x=0 \ .$$

Here $\mathcal{L}_K$ is a Lie differentiation in the Killing direction; only $\mathcal{L}_z=\partial/\partial z$ is nonzero in our case, and $(\delta g_{ij}^{TT})\propto h_1$ and $\delta\pi^{ijTT}\propto\hat{\eta}_1$. Brill's result is then identical to our Eq. (3.18). Notice that Eq. (2.14b) requires that the full (nonlinear) variables satisfy $\oint(h^{3/2})'\hat{\eta}_* dz=-\oint(h^{3/2})\hat{\eta}'_* dz=0$.

Finally, we can write the second-order Hamiltonian constraint:

$$\begin{aligned}\phi''_2=&-h'_1\phi'_1-\tfrac{1}{4}(\phi_1h''_1+h''_2-h_1h''_1)\\ &+f(t)(\phi_2-\tfrac{3}{2}\phi_1^2-\tfrac{1}{8}\hat{\eta}_2-\tfrac{1}{16}\hat{\eta}_1^2+\tfrac{7}{8}\phi_1\hat{\eta}_1\\ &-\tfrac{1}{24}\hat{A}_2-\tfrac{1}{48}\hat{A}_1^2+\tfrac{7}{24}\phi_1\hat{A}_1) .\end{aligned} \tag{3.19}$$

Equation (3.19) has been simplified, in particular taking account of the second-order momentum constraint.

Before proceeding, we make a semantic point which will greatly simplify subsequent equations. The important point is that we are completely free to set h and $\hat{\eta}$. They are totally unconstrained in the full equations as we pose them; they determine the sources for the constrained variables ϕ and $\hat{A}$. Hence we can *a priori* set $h_n=0$, $\hat{\eta}_n=0$, $n>1$; the function h to all orders is set by giving its first nonconstant term, the same for $\hat{\eta}$. This is just a question of semantics, which, however, simplifies the Eqs. (3.16) and (3.19).

IV. SOME ANALYTIC SOLUTIONS

In this section we present some analytic solutions to the field equations derived above. Since we work at a fixed time t, we can choose $t=1$. Then the perturbation equations for the flat and the cosmological initial data problems become identical. The two systems differ only because the value of the zero-order (unperturbed) variables differs in the two cases, and this difference propagates into the higher-order perturbations.

We first present an analytical second-order solution, beginning with the momentum constraint. The full nonlinear momentum constraint has the solution

$$(\hat{A}h^{3/2})=-\tfrac{1}{2}\int_0^z h^{1/2}h'\hat{\eta}dz+C(t) \ , \tag{4.1}$$

where $\hat{\eta}$ and h are the full nonlinear free variables. The integrand must be such that $\int_0^L hh^{1/2}\hat{\eta}'dz=0$; this periodicity is the full nonlinear expression of "linearization stability." The function $C(t)$ is of course constant on each constant mean curvature slice. On the initial slice, a choice must be made for C. This constant extends to the perturbed case the invariance of the metric to constants added in h_1 at one time. The specification of C is a gauge choice. As we compare the behavior of perturbations of different amplitude, we need a prescription for this specification. This is essential to specify *homogeneous* modes in the deviation from the background. We present our choice of C on the initial slice by considering the momentum constraint order by order. At first order we have, from Eq. (3.11),

$$\hat{A}_1 = -3h_1 + C_1 + 3h_1(0,t_0) \ , \tag{4.2}$$

where the constant $3h_1(0,t_0)$ is included; note that the choice $C_1=0$ makes $\hat{A}_1$ vanish at the point $z=0$. This solution can then be used to solve Eq. (3.16) for the second-order perturbation quantity $\hat{A}_2$:

$$\begin{aligned}\hat{A}_2 = {} & \tfrac{15}{4}h_1^2 - \tfrac{15}{4}h_1^2(0,t_0) - \tfrac{3}{2}[C_1 + 3h_1(0,t_0)]h_1 \\ & + \tfrac{3}{2}[C_1 + 3h_1(0,t_0)]h_1(0,t_0) \\ & - \tfrac{3}{2}\int_0^z \hat{\eta}_1 h_1' dz + C_2 \ .\end{aligned} \tag{4.3}$$

Note that we have set $h_2=0$ as discussed above. Regardless of our choice setting $h_2=0$, one can introduce terms in $\hat{A}_2$ that have the same period as does h_1; these arise from the constant $-\frac{3}{2}[C_1+3h_1(0,t_0)]h_1$ term in Eq. (4.3). The gauge choice for C_1, the integration constant at first order, affects this constant.

From the results (4.2) and (4.3) we can specify a set of choices to simplify these equations, and the Hamiltonian constraint (see below). These choices are

$$3h_1(0,t_0) + C_1 = 0 \ , \tag{4.4}$$

$$-\tfrac{15}{4}h_1^2(0,t_0) + C_2 = 0 \ . \tag{4.5}$$

Thus,

$$\hat{A}_1 = -3h_1 \ , \tag{4.6}$$

$$\hat{A}_2 = \tfrac{15}{4}h_1^2 - \tfrac{3}{2}\int_0^z \hat{\eta}_1 h_1' dz \ . \tag{4.7}$$

More explicit solution of these equations requires a definite specification of the form of $\hat{\eta}_1$ and h_1. We note that although these additive constant choices (4.4) and (4.5) can be made on the initial slice, maintenance of these choices will amount to dictating the shift vector, a subject we will not pursue in this paper.

Because of the form of the equation for $\hat{A}$, together with the linear form $\hat{\eta} = \sigma(1+\hat{\eta}_1)$ for $\hat{\eta}$, where $\sigma=+1$ for the flat case and $\sigma=-1$ for the cosmology, the *lowest-order* terms for $\hat{A}$ can be evaluated directly from the full momentum constraint equation (4.1):

$$\hat{A} = -\sigma\tfrac{1}{2}h^{-3/2}\int_0^z \tfrac{2}{3}(h^{3/2})'(1+\hat{\eta}_1)dz + \tilde{\tilde{\tilde{A}}}_0 h^{-3/2} \tag{4.8a}$$

$$= -\frac{\sigma}{3} - \frac{\sigma}{3}h^{-3/2}\int_0^z (h^{3/2})'\hat{\eta}_1 dz + \tilde{\tilde{A}}_0 h^{-3/2} \tag{4.8b}$$

$$= -\frac{\sigma}{3} - \frac{\sigma}{3}\hat{\eta}_1 + \tfrac{1}{3}h^{-3/2}\left[\sigma\int_0^z h^{3/2}\hat{\eta}_1' dz + \tilde{A}_0\right] \tag{4.8c}$$

$$= -\frac{\sigma}{3} - \frac{\sigma}{3}\hat{\eta}_1 + (\tfrac{1}{3} - \tfrac{1}{2}h_1 + \tfrac{5}{8}h_1^2)\left[\sigma\int_0^z (1+\tfrac{3}{2}h_1)\hat{\eta}_1' dz + \tilde{A}_0\right] \ . \tag{4.8d}$$

Notice from Eqs. (3.8) that $\hat{A} = (\sigma/3)(1+\hat{A}_1+\hat{A}_2)$, and the unperturbed value $\hat{A} = \sigma/3$, so the constant $\tilde{A}_0$ must be chosen as $\tilde{A}_0 = 2\sigma$ to give the correct zero-order limit. Eq. (4.8d) is then a solution to the momentum constraint to second order in a form that is often more convenient than summing Eqs. (4.6) and (4.7).

We now turn to a consideration of the second-order Hamiltonian constraint. The solution of Eq. (3.19) is straightforward. The equation is rewritten so that on the left-hand side (LHS) only the linear operator appears:

$$\text{LHS} = \phi_2'' - \phi_2 f(t) \ . \tag{4.9}$$

The quantities on the right-hand side are now $\hat{A}_2$, which arises from a nonlinear combination of $\hat{\eta}_1$ and h_1, and other quadratic combinations of $\hat{\eta}_1$ and h_1. Since we deal with solutions on a finite $[0,L]z$ axis, each variable has a discrete Fourier series. Thus each of these quadratic terms on the right-hand side can be expanded in a Fourier series and

$$\begin{aligned}\text{RHS} &= \sum_{l=0}^{\infty} (\text{RHS})_l \\ (\text{RHS})_l &= a_l \sin\left[\frac{2\pi l z}{L} + \delta_{ls}\right] + b_l \cos\left[\frac{2\pi l z}{L} + \delta_{lc}\right] \ ,\end{aligned} \tag{4.10}$$

where δ_{ls} and δ_{lc} are phases. The solution to Eq. (3.19) is then, trivially,

$$\phi_2 = -\sum_{l=0}^{\infty} \frac{(\text{RHS})_l}{\left[\dfrac{2\pi l}{L}\right]^2 + f(t)} \ . \tag{4.11}$$

More detail requires a specification of the particular problem. For a first example we consider

$$h=1+a\sin nz\ , \tag{4.12a}$$

$$\hat{\eta}=\sigma(1+b\sin nz) \tag{4.12b}$$

with n chosen such that $n=2\pi l/L$ where l is some integer. Direct integration of Eq. (4.8a) with Eq. (4.12) leads to the full solution

$$\begin{aligned}\sigma\hat{A}&=\tfrac{1}{3}(1+\hat{A}_1+\hat{A}_2+\cdots)\\&=-\tfrac{1}{3}-\tfrac{1}{3}b\sin nz\\&\quad+\frac{2}{15}\frac{b}{a}[(1+a\sin nz)-(1+a\sin nz)^{-3/2}]\\&\quad+\tfrac{2}{3}(1+a\sin nz)^{-3/2}\ .\end{aligned} \tag{4.13}$$

Expanding out the remaining $h^{-3/2}$ to second order, one finds, for this case,

$$\begin{aligned}&\hat{A}_0=1\ ,\\&\hat{A}_1=-3a\sin nz\ ,\\&\hat{A}_2=3\left[\frac{5}{4}a^2-\frac{ba}{4}\right]\sin^2 nz\ .\end{aligned} \tag{4.14}$$

As a further check, the results $\hat{A}_1$ and $\hat{A}_2$ in Eq. (4.14) are consistent with the first- and second-order equations (4.6) and (4.7). This solution for $\hat{A}$ is discussed further in Sec. V (cf. Tables I and II and Fig. 2 below).

To solve for ϕ, we cannot give an explicit solution but must do the perturbation expansion. We obtain the first-order correction to ϕ from Eq. (3.10):

$$\begin{aligned}[\phi_1''-f(t)\phi_1]&=+\tfrac{1}{4}an^2\sin nz+f(t)(\tfrac{1}{8}a\sin nz-\tfrac{1}{8}b\sin nz)\\&=\frac{1}{4}\left[an^2+f(t)\left[\frac{a}{2}-\frac{b}{2}\right]\right]\sin nz\ ,\end{aligned} \tag{4.15}$$

where we inserted the forms for h, $\hat{\eta}_1$, and $\hat{A}_1$. Hence ϕ_1 is proportional to $\sin nz$; $\phi_1=j\sin nz$ with

$$j=\frac{-\tfrac{1}{4}[an^2+f(t)(a/2-b/2)]}{n^2+f(t)}\ . \tag{4.16}$$

The second-order computation is similar but of course more complicated [from Eq. (3.19)]. We see that the second-order source for ϕ_2 consists of terms $\propto\cos^2 nz$ and terms $\propto\sin^2 nz$, which yields

$$\phi_2=\left[\frac{an^2j+e}{2f(t)}-\frac{1}{2}\left[\frac{e-jan^2}{4n^2+f(t)}\right]\cos 2nz\right]\ , \tag{4.17}$$

where

$$\begin{aligned}e&=\tfrac{1}{4}(a^2-ja)n^2\\&\quad+f(t)[\tfrac{3}{2}j^2+\tfrac{1}{32}(11a^2+2b^2-ba)+\tfrac{7}{8}(a-b)j]\ .\end{aligned} \tag{4.18}$$

This solution for ϕ is discussed in Sec. V (cf. Tables V and VI and Fig. 3 below).

The only other analytical exact solution we present involves data for h and $\hat{\eta}$ with different wave numbers. We take

$$h=1+a\sin nz,\quad \hat{\eta}=\sigma(1+b\sin 3nz)\ . \tag{4.19}$$

We solve for $\hat{A}$ from Eq. (4.8c). Because

$$\hat{\eta}'=\sigma 3nb\cos 3nz=\sigma 3nb(1-4\sin^2 nz)\cos nz\ ,$$

we must evaluate two integrals:

$$\begin{aligned}3h^{3/2}&\left[\hat{A}+\frac{\sigma}{3}+\frac{\sigma}{3}\hat{\eta}_{(1)}\right]\\&=\sigma\int(1+a\sin nz)^{3/2}3nb(1-4\sin^2 nz)\cos nz\,dz+\hat{A}_0\\&=\sigma I_1+\sigma I_2+\hat{A}_0\ ,\end{aligned} \tag{4.20}$$

where (using $x=a\sin nz$)

$$\begin{aligned}I_1&=\frac{3b}{a}\int_0^{x=a\sin nz}(1+x)^{3/2}dx\\&=\frac{2}{5}\frac{3b}{a}[(1+a\sin nz)^{5/2}-1]\end{aligned} \tag{4.21}$$

and

$$\begin{aligned}I_2&=-\frac{12b}{a^3}\int_0^{x=a\sin nz}(1+x)^{3/2}x^2dx\\&=-\frac{12b}{a^3}\{\tfrac{2}{9}[(1+a\sin nz)^{9/2}-1]\\&\qquad-\tfrac{4}{7}[(1+a\sin nz)^{7/2}-1]\\&\qquad+\tfrac{2}{5}[(1+a\sin nz)^{5/2}-1]\}\ .\end{aligned} \tag{4.22}$$

From Eqs. (4.20), (4.21), and (4.22) we can reconstruct $\hat{A}$; recall that we must set $\tilde{A}_0=2\sigma$. Even though the integrated forms of Eqs. (4.21) and (4.22) have inverse powers of a, they do in fact have finite limits (tending to zero) for $a\to 0$. The forms of the integrals with their limits show that the integral in Eq. (4.21) is proportional to a; the integral in Eq. (4.22) is proportional to a^3; and

$$\begin{aligned}&\hat{A}_0=1,\quad \hat{A}_1=-3a\sin nz\ ,\\&\hat{A}_2=\tfrac{15}{4}a^2\sin^2 nz-\tfrac{9}{4}ba\sin^2 nz(1-\tfrac{2}{3}\sin^2 nz)\ .\end{aligned} \tag{4.23}$$

The first-order ϕ perturbation is, from Eq. (3.10),

$$\phi_1=-\frac{n^2a/4+f(t)a/8}{n^2+f(t)}\sin nz+\frac{(b/8)f(t)}{9n^2+f(t)}\sin 3nz\ . \tag{4.24}$$

Because of its complexity, we will not give the explicit second order for ϕ_2; the general form is given by Eq. (4.17). Notice that we are in any case completely able to integrate the Hamiltonian constraint, explicitly demonstrating that there is no linearization instability arising from that equation. This solution is further discussed in Sec. V. see also Tables III, IV, VII, and VIII below.

The linearization stability condition from the momentum constraint Eq. (3.18) is, as we have noted, only the lowest-order version of this condition. The full periodicity requirement for $\hat{A}$ is that

$$\int_0^L(h^{3/2})'\hat{\eta}_*dz=\oint(h^{3/2})'\hat{\eta}_*dz=0\ . \tag{4.25}$$

Now

$$\oint (h^{3/2})'\hat{\eta}_* dz = \oint (h^{3/2}\hat{\eta}_*)'dz - \oint h^{3/2}\hat{\eta}_*'dz \ ; \qquad (4.26)$$

but because these are closed-loop integrals, the first term on the right vanishes identically, and full periodicity can be restated:

$$\oint h^{3/2}\hat{\eta}'_* dz = 0 \ . \qquad (4.27)$$

One way of expressing this condition is similar to Eqs. (3.12) and (3.13):

$$h^{3/2} = \sum (h^{3/2})_m \sin(2\pi m z/L + \delta_{(m)}) \ , \qquad (4.28a)$$

$$\hat{\eta}_* = \sum \hat{\eta}_m \sin(2\pi m z/L + \delta_{(m)}) \ , \qquad (4.28b)$$

where the $\delta_{(m)}$ are the same function of m in each case. Another approach, of use if $\hat{\eta}$ and h are taken as single-mode quantities, is to write (at time $t=1$)

$$h = 1 + a \sin 2\pi n_h z/L$$

and to then expand $h^{3/2}$ by the binomial expansion. (Perforce $|a|<1$ or the metric is singular.) The expansion of $h^{3/2}$ will contain all powers of $\sin 2\pi n_h z/L$. From Gradshteyn and Rhyzik,[26] we have

$$\sin^{2n} x = \frac{1}{2^{2n}} \left[\sum_{k=0}^{n-1} (-1)^{n-k} 2 \begin{bmatrix} 2n \\ k \end{bmatrix} \cos 2(n-k)x + \begin{bmatrix} 2n \\ n \end{bmatrix} \right], \qquad (4.29a)$$

$$\sin^{2n-1} x = \frac{1}{2^{2n-2}} \sum_{k=0}^{n-1} (-1)^{n+k-1} \begin{bmatrix} 2n-1 \\ k \end{bmatrix} \times \sin(2n-2k-1)x \ . \qquad (4.29b)$$

Hence the expansion of $h^{3/2}$ contains cosines of all even multiples of $2\pi n_h z/L$, and the sines of all odd multiples of $2\pi n_h z/L$. We wish Eq. (4.27) to hold, which is now a simple question of the orthogonality of trigonometric functions. We see that the full version of linearization stability fails, in the single-mode case, if

$$\hat{\eta} \propto \sin p n_h z \frac{2\pi}{L} \ , \qquad (4.30a)$$

where p is an even positive integer, and when

$$\hat{\eta} \propto \cos p n_h z \frac{2\pi}{L} \ , \qquad (4.30b)$$

where p is an odd positive integer.

These conditions reduce to the linearization stability condition of Eqs. (3.12) and (3.13) in the lowest-order limit where they refer only to the $p=1$ case. We had to take care in our numerical solutions that these conditions were obeyed in their full nonlinear form. The deviation from periodicity in $\hat{A}$ arising from violating these conditions beyond the lowest order [Eq. (4.25)] arose predictably in our numerical work at order $a^p b$, where a is the amplitude of the deviation of h from unity, b is the deviation of $\hat{\eta}$ from unity, and p is the order that enters Eqs. (4.30a) and (4.30b).

V. NUMERICAL SOLUTIONS AND CODE TESTS

Here we present the numerical techniques used to solve the momentum and Hamiltonian constraint equations. In both cases, the numerical solutions are compared to analytic solutions in the full nonperturbative regime. Calibrating the code against such test-bed calculations is critical to making it a reliable tool for exploring the parameter space of the initial-value equations.

The numerical grid is shown in Fig. 1. The z direction is covered with two sets of coordinates: ZA_k at zone faces and ZB_k at zone centers, where $k=1,2,\ldots,km$. Note that the zoning need not be uniform; however, the examples we present here all use uniform zoning. We impose periodic boundary conditions by identifying quantities at $k=1$ and $km-1$ and at $k=2$ and km, and by carrying dummy zones as shown in Fig. 1. Note that $z=0$ has been chosen to lie at ZB_2 and $z=L$ at ZB_{km}. Thus in the range $[0,L]$ there are $km-1$ nodes ZB_k, including the nodes ZB_2 and ZB_{km}, and $km-2$ zones DZB_k. The quantities $\hat{A}$, h, $\hat{\eta}$, and ϕ are defined at zone center ZB_k.

The momentum constraint is straightforward to solve since it is linear in the variable $\hat{A}$. From Eq. (4.1) we have

$$\hat{A} = -\tfrac{1}{2} h^{-3/2} \int_0^z h^{1/2} h' \hat{\eta} dz + h^{-3/2} C(t) \ , \qquad (5.1)$$

where

$$C(t) = (\hat{A} h^{3/2})_{z=0,t} \ . \qquad (5.2)$$

On the initial slice, the value of the integration constant $C(t)$ is set by our choice of the free data h and the boundary condition for $\hat{A}$ at $z=0$. On subsequent slices the value of $h(z=0)$ will come from the evolution equation for h, and $\hat{A}(z=0)$ will come from a condition imposing periodicity on the shift vector.[20]

The integral in Eq. (5.1) is solved by converting it into a sum and finding the area under the curve using a trapezoidal rule. Letting the integrand

$$u = h^{1/2} h' \hat{\eta} \qquad (5.3)$$

be defined at ZB_k we have

$$\mathcal{J} = \int_{ZB_2}^{ZB_k} u dz \ , \qquad (5.4)$$

which becomes

$$\mathcal{J}_k = \tfrac{1}{2} \sum_{j=3}^{k} (u_j DZA_j + u_{j-1} DZA_{j-1}) \qquad (5.5)$$

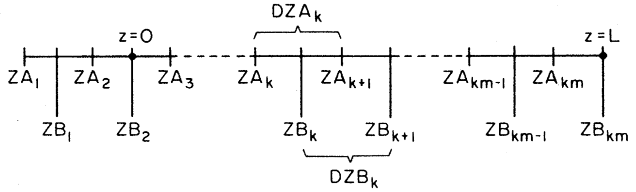

FIG. 1. The numerical grid. Nodes at $k=1$ and $km-1$ and at $k=2$ and km are identified to produce periodic boundary conditions. The quantities $\hat{A}$, h, $\hat{\eta}$, and ϕ are defined at ZB_k.

TABLE I. Error indicators for solving the momentum constraint for $\hat{A}$ using 128 nodes. In this case the free data h and η have equal amplitudes and wavelengths $\lambda_h=\lambda_{\hat{\eta}}=L$. This problem has an analytic solution, Eq. (4.13), which was used to form the error indicators.

Amplitude a of free data	$\text{error}_{\text{zone,abs}}$	$\text{error}_{\text{cum,rel}}$
0.001	3×10^{-7}	6×10^{-7}
0.01	3×10^{-6}	6×10^{-6}
0.1	3×10^{-5}	6×10^{-5}
0.5	1×10^{-4}	1×10^{-4}
0.8	2×10^{-4}	6×10^{-5}
0.9	1×10^{-3}	7×10^{-5}

TABLE III. Error indicators for solving the momentum constraint for $\hat{A}$ using 128 nodes. Here the free data h and η have equal amplitudes but unequal wavelengths $\lambda_h=3\lambda_{\hat{\eta}}=L$. The analytic solution (4.23) was used to form the error indicators.

Amplitude a of free data	$\text{error}_{\text{zone,abs}}$	$\text{error}_{\text{cum,rel}}$
0.001	3×10^{-7}	6×10^{-7}
0.01	3×10^{-6}	6×10^{-6}
0.1	3×10^{-5}	6×10^{-5}
0.5	2×10^{-4}	2×10^{-4}
0.8	1×10^{-3}	3×10^{-4}
0.9	5×10^{-3}	4×10^{-4}

for $k=3,\ldots,km$; we define $\mathcal{J}_2=0$. We verify periodicity of this scheme by checking to see that $\mathcal{J}_{km}=\mathcal{J}_2$. We then use Eq. (5.1) to get

$$\hat{A}_k=h_k^{-3/2}(-\tfrac{1}{2}\mathcal{J}_k+C)\ . \tag{5.6}$$

To quantify the comparison between numerical and analytic solutions we monitor two error indicators. In the first, we calculate the absolute error in each zone for some function f and then take the maximum over the grid:

$$\text{error}_{\text{zone,abs}}=\text{max}_{\text{over grid}}|f_{\text{computed},k}-f_{\text{analytic},k}|\ . \tag{5.7}$$

We also look at a relative cumulative error over the grid using

$$\text{error}_{\text{cum,rel}}=\left[\frac{\sum_{\text{grid}}|f_{\text{computed},k}-f_{\text{analytic},k}|^2}{\sum_{\text{grid}}f^2_{\text{analytic},k}}\right]^{1/2}\ . \tag{5.8}$$

These errors are to be compared with the expected truncation errors.

To test the algorithm (5.6) we choose free data in the form used to derive the perturbative and full analytic solutions in Sec. IV for the case of a flat-space background ($\sigma=1$). As a first example we use free data in the form given by Eq. (4.12), in which h_1 and $\hat{\eta}_1$ both have wavelengths equal to the size of the grid L and equal amplitudes $a=b$ that vary in the range [0.001,0.9]. The results of solving for $\hat{A}$ numerically using a grid covered by 128 nodes and 1280 nodes are shown in Tables I and II, respectively, where the full analytic solution (4.13) has been used to compute the error indicators. We also consider the case of different wavelengths in h_1 and $\hat{\eta}_1$ using Eq. (4.19) with wavelengths $\lambda_h=3\lambda_{\hat{\eta}}=L$ and equal amplitudes $a=b$. The comparison of the analytic solution, given by Eqs. (4.20)–(4.22), with the computed solution is shown in Table III for a grid with 128 nodes and in Table IV for 1280 nodes.

The error indicators given in Tables I–IV behave as expected. For example, the truncation errors[27] scale $\sim(\Delta z)^2$; thus the error indicators should decrease $\sim(\Delta z)^2$ as the resolution of the grid increases. This can be seen from a comparison between Tables I and II and between Tables III and IV where the sizes of the errors drop by a factor $\sim10^2$ as the number of zones increases by a factor of 10. Also, note that the values of the error indicators increase within each table as the amplitude of the free data increases. This is due to the fact that $\hat{A}$ steepens and changes in shape as the input amplitude is increased, producing an asymmetric profile with a narrow pulse on one side of the grid; this can be seen in Figs. 2(a)–2(e). This steepening and narrowing of the profile leads to an effective lowering of the resolution in that region of the grid. Finally, the errors for the case of unequal wavelengths are slightly larger than those for the case of equal wavelengths. This is due to the presence of shorter wavelengths, which also effectively lowers the resolution.

We turn now to the nonlinear Hamiltonian constraint. The existence and uniqueness of a positive bounded solution to this equation have been demonstrated by O'Murchadha and York.[28] In finding this solution we follow a strategy based on that developed by Evans.[3] The first step is to linearize the equation about some solution ϕ_0. The resulting linear equation is solved using an optimized incomplete Cholesky conjugate-gradient (ICCG)

TABLE II. Free data h and η have equal amplitudes and wavelengths $\lambda_h=\lambda_{\hat{\eta}}=L$ (same as Table I) but for 1280 nodes.

Amplitude a of free data	$\text{error}_{\text{zone,abs}}$	$\text{error}_{\text{cum,rel}}$
0.001	3×10^{-9}	6×10^{-9}
0.01	3×10^{-8}	6×10^{-8}
0.1	3×10^{-7}	6×10^{-7}
0.5	1×10^{-6}	1×10^{-6}
0.8	2×10^{-6}	6×10^{-7}
0.9	1×10^{-5}	7×10^{-7}

TABLE IV. Same as Table III but for 1280 nodes.

Amplitude a of free data	$\text{error}_{\text{zone,abs}}$	$\text{error}_{\text{cum,rel}}$
0.001	2×10^{-8}	2×10^{-8}
0.01	3×10^{-8}	6×10^{-8}
0.1	3×10^{-7}	6×10^{-7}
0.5	2×10^{-6}	2×10^{-6}
0.8	1×10^{-5}	3×10^{-6}
0.9	5×10^{-5}	4×10^{-6}

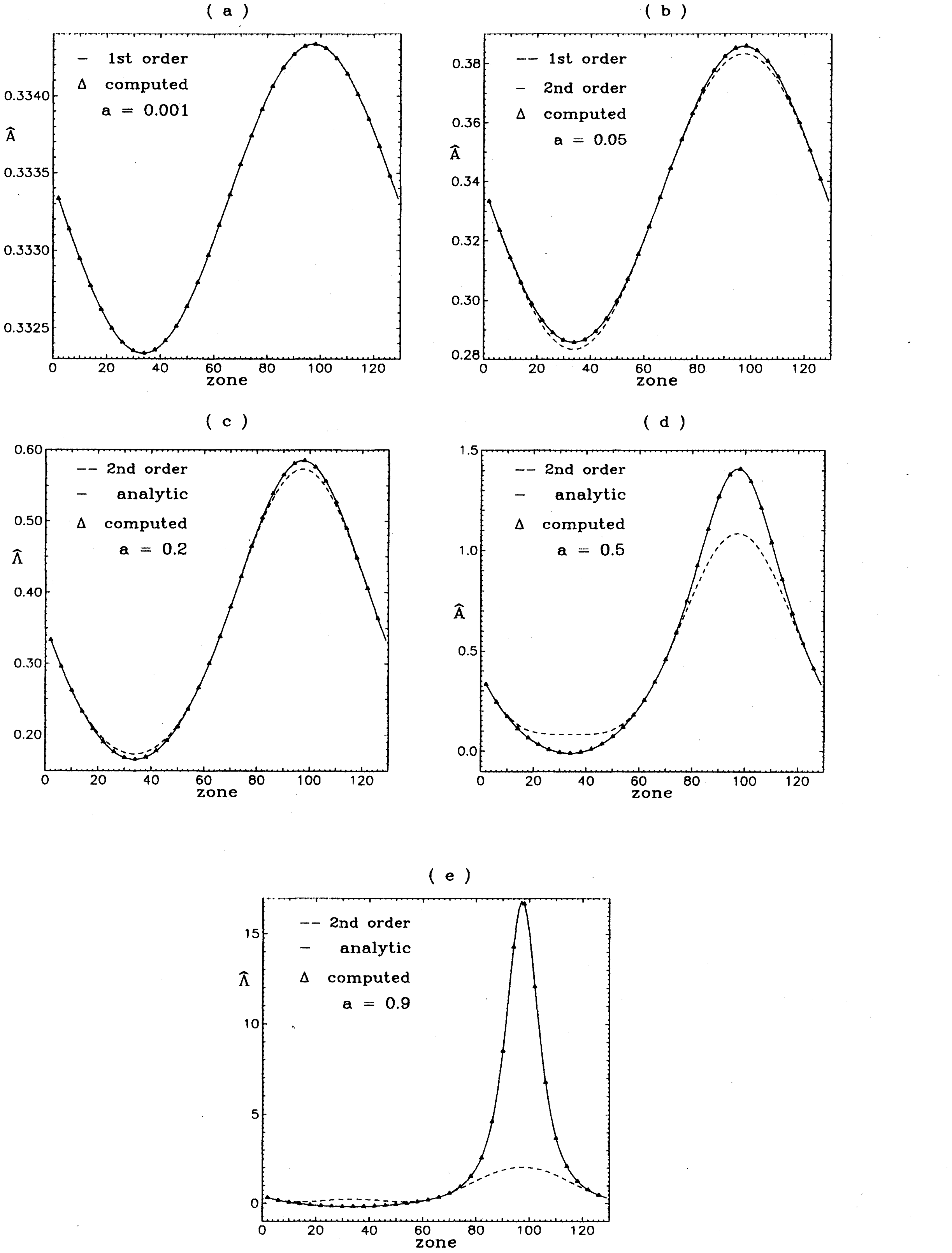

FIG. 2. Perturbative, exact analytic, and code solutions for $\hat{\Lambda}$ for the case of free data with equal amplitudes and wavelengths $\lambda_h=\lambda_{\hat{\eta}}=L$. See Eqs. (4.12)–(4.18) and Sec. V. The numerical grid has 128 nodes, and every fourth value of the code solution is plotted.

matrix solver, which has been shown to converge rapidly.[3,29] The solution thus obtained is used as the new value of ϕ_0, and this cycle is repeated until successive iterations produce convergence to a solution. To guard against blunders, this solution is then checked to see if it solves the full nonlinear equation.

With the definitions

$$M=-\tfrac{1}{4}h'' , \tag{5.9a}$$

$$B=\tfrac{1}{12}(\mathrm{tr}K)^2h , \tag{5.9b}$$

and

$$S=-\tfrac{1}{16}(\hat{\eta}^2+3\hat{A}^2)h \tag{5.9c}$$

the Hamiltonian constraint (2.15) becomes

$$(\phi'h)'=M\phi+B\phi^5+S\phi^{-7} . \tag{5.10}$$

Linearizing about some solution ϕ_0,

$$\phi=\phi_0+\delta\phi , \tag{5.11}$$

Eq. (5.10) becomes

$$(\phi'h)'=D\phi+E , \tag{5.12}$$

where

$$D=M+5B\phi_0^4-7S\phi_0^{-8} \tag{5.13a}$$

and

$$E=8S\phi_0^{-7}-4B\phi_0^5 . \tag{5.13b}$$

To discretize Eq. (5.12) we note that $\hat{A}$, $\hat{\eta}$, h, and ϕ lie at zone center ZB_k. Writing

$$F_k=\frac{h_{k+1}+h_k}{2DZB_k} \tag{5.14}$$

we get

$$(\phi'h)'_k=\frac{1}{DZA_k}[F_k\phi_{k+1}-(F_k+F_{k-1})\phi_k+F_{k-1}\phi_{k-1}] . \tag{5.15}$$

Discretizing the right-hand side of Eq. (5.12) at ZB_k and using Eq. (5.15) then gives

$$G_k=F_k\phi_{k+1}-H_k\phi_k+F_{k-1}\phi_{k-1} , \tag{5.16}$$

where

$$H_k=F_k+F_{k-1}+D_kDZA_k \tag{5.17a}$$

and

$$G_k=E_kDZA_k . \tag{5.17b}$$

Applying periodic boundary conditions, Eq. (5.16) can be written as a banded symmetric matrix equation with two off-diagonal terms:

$$\begin{bmatrix} -H_2 & F_2 & & & & & F_{km-1} \\ F_2 & -H_3 & F_3 & & & & \\ & F_3 & -H_4 & F_4 & & & \\ & & \vdots & \vdots\ \vdots & \vdots & & \\ & & & & F_{km-3} & -H_{km-2} & F_{km-2} \\ F_{km-1} & & & & & F_{km-2} & -H_{km-1} \end{bmatrix} \begin{bmatrix} \phi_2 \\ \phi_3 \\ \phi_4 \\ \vdots \\ \phi_{km-2} \\ \phi_{km-1} \end{bmatrix} = \begin{bmatrix} G_2 \\ G_3 \\ G_4 \\ \vdots \\ G_{km-2} \\ G_{km-1} \end{bmatrix} . \tag{5.18}$$

Equation (5.18) can now be solved using an ICCG solver optimized for the computer in use, here a Cray X/MP.

Our procedure works as follows. Begin by choosing an initial guess solution ϕ_0. For these initial-value problems, we choose ϕ_0 to be a constant in the range [1,10]. The larger values of ϕ_0 are necessary to obtain a positive-definite solution for large perturbations in the free data; the solutions would otherwise converge to the negative image of the positive-definite solution. (This property is indicated in the reflection symmetry of the Hamiltonian constraint equation, which remains invariant under the change of sign $\phi\rightarrow-\phi$.) Using ϕ_0, solve Eq. (5.18) for ϕ; this process usually converges to better than 1 part in 10^{10} in approximately 2–3 iterations. Now set the new ϕ equal to ϕ_0 and repeat. In all cases tried, this process converges, i.e., $\phi_0=\phi$, to 10^{-10} after about 5–10 iterations. Finally, we make a direct comparison of the left-hand side $[(\phi'h)']$ and the right-hand side $(M\phi+B\phi^5+S\phi^{-7})$ of the full nonlinear Hamiltonian constraint (5.10). The maximum deviation (LHS−RHS) was monitored and found to be less than 10^{-10} in all cases. Note that this deviation is an estimate of the error in the solution to the *difference* equation. We must still find analytic test-bed solutions to the Hamiltonian constraint in order to check the effects of truncation error.

In the first- and second-order perturbative regimes we can use the analytic solutions derived in Sec. IV for comparison with the numerical results. For the case of free data in the form (4.12) with equal amplitudes $a=b$ and wavelengths $\lambda_h=\lambda_{\hat{\eta}}=L$, the conformal factor can be written to second order $\phi=1+\phi_1+\phi_2$ using Eqs. (4.16)–(4.18). Comparing the analytic solution to second

TABLE V. Error indicators for solving the Hamiltonian constraint for ϕ using 128 nodes. In this case the free data h and η have equal amplitudes and wavelengths $\lambda_h = \lambda_{\hat{\eta}} = L$. These results correspond to the same solution for which $\hat{A}$ errors appear in Table I. The second-order analytic solution (4.16)–(4.18) was used to form the error indicators.

Amplitude a of free data	$\mathrm{error}_{\mathrm{zone,abs}}$	$\mathrm{error}_{\mathrm{cum,rel}}$
0.001	2×10^{-9}	1×10^{-9}
0.01	5×10^{-7}	3×10^{-7}
0.1	9×10^{-4}	5×10^{-4}

TABLE VII. Same as Table V but for the case in which the free data have equal amplitudes but different wavelengths $\lambda_h = 3\lambda_{\hat{\eta}} = L$. These 128 node results correspond to the same solution for which $\hat{A}$ errors appear in Table III. The first-order analytic result, Eq. (4.24), and its second-order extension were used to form the error indicators.

Amplitude a of free data	$\mathrm{error}_{\mathrm{zone,abs}}$	$\mathrm{error}_{\mathrm{cum,rel}}$
0.001	1×10^{-9}	9×10^{-10}
0.01	5×10^{-7}	3×10^{-7}
0.1	9×10^{-4}	5×10^{-4}

order with the code solution produces the error indicators shown in Table V for a grid with 128 nodes and in Table VI for 16 nodes. Similarly, the case of equal amplitudes and different wavelengths $\lambda_h = 3\lambda_{\hat{\eta}} = L$ produces the results in Table VII for 128 nodes and in Table VIII for 16 nodes.

The error indicators in Tables V–VIII behave as expected. Increasing the amplitude of the free data effectively lowers the resolution of the calculation; this effect is seen in both the absolute and relative errors within each of the Tables V–VIII for the cases $a = 0.001$ and $a = 0.01$. The substantial increase in error between $a = 0.01$ and $a = 0.1$ is due to the fact that this marks the transition out of the second-order regime; cf. Figs. 3(b) and 3(c). In addition, the errors should decrease by a factor $\sim 10^2$ as the number of nodes goes from 16 to 128, since we are using centered differences with truncation errors that scale $\sim (\Delta z)^2$. This is observed in the case $a = 0.001$. However, we see only a factor ~ 10 decrease for $a = 0.01$. This is due to the fact that the analytic solution for ϕ to second order has leading error terms $\sim h_1^3 \sim 10^{-6}$ for $a = 0.01$. Since the numerical errors are also $\sim 10^{-6}$, the effect of the scaling $\sim (\Delta z)^2$ is mostly lost. Similarly, the case $a = 0.001$ has leading error terms in the analytic solution $\sim h_1^3 \sim 10^{-9}$. Increasing the number of nodes from 128 to 1280 cannot be expected to improve the errors; we have verified that this is in fact what happens.

We also need a test of the Hamiltonian constraint in the nonperturbative regime. To find such a solution we use a technique suggested by Evans.[30] The idea is to give values for h, $\hat{A}$, and ϕ and use these to solve the Hamiltonian constraint analytically for $\hat{\eta}$. This produces a consistent analytic solution for ϕ. Now use these values of h, $\hat{A}$, and $\hat{\eta}$ and solve the Hamiltonian constraint for ϕ numerically. Comparison between the computed and analytic values of ϕ then yields a test of the code.

To implement this procedure we choose

$$h = h_0 = \text{const} \; ; \tag{5.19}$$

the momentum constraint then requires

$$\hat{A} = \hat{A}_0 = \text{const} \; . \tag{5.20}$$

With these values and the choice

$$\phi = \phi_0 + b \sin nz \; , \tag{5.21}$$

where $n = 2\pi m / L$ and m is some integer, the Hamiltonian constraint becomes an algebraic equation for $\hat{\eta}$. The solution is

$$\hat{\eta} = \left[16(bn^2 \sin nz)(\phi_0 + b \sin nz)^7 + \frac{4(\mathrm{tr}K)^2}{3}(\phi_0 + b \sin nz)^{12} - 3\hat{A}_0^2 \right]^{1/2} \; . \tag{5.22}$$

Note that Eq. (5.22) imposes a constraint on h_0, $\hat{A}_0$, ϕ_0, n, b, and $\mathrm{tr}K$, since $\hat{\eta}^2 \geq 0$.

Now use the above solutions for h, $\hat{A}$, and $\hat{\eta}$ and solve numerically for ϕ. We choose

$$\phi_0 = 10, \quad h_0 = 1, \quad \hat{A}_0 = 1 \; ,$$

and

$$\mathrm{tr}K = 200 \; ,$$

and let b vary in the range [0.01,9]. The large value of $\mathrm{tr}K$ is the result of satisfying $\hat{\eta}^2 \geq 0$. The Hamiltonian constraint is solved for ϕ and this value is compared with the analytic solution (5.21).

We consider two cases, $m = 1$ and $m = 3$. Tables IX and X contain the error indicators for the case $m = 1$ using 128 and 16 nodes, respectively. The case $m = 3$ is shown in Tables XI and XII using 128 and 16 nodes, respectively. As expected, increasing the amplitude of the

TABLE VI. Same as Table V but for 16 nodes.

Amplitude a of free data	$\mathrm{error}_{\mathrm{zone,abs}}$	$\mathrm{error}_{\mathrm{cum,rel}}$
0.001	2×10^{-7}	1×10^{-7}
0.01	3×10^{-6}	2×10^{-6}
0.1	7×10^{-4}	4×10^{-4}

TABLE VIII. Same as Table VII but for 16 nodes.

Amplitude a of free data	$\mathrm{error}_{\mathrm{zone,abs}}$	$\mathrm{error}_{\mathrm{cum,rel}}$
0.001	1×10^{-7}	9×10^{-8}
0.01	3×10^{-6}	2×10^{-6}
0.1	7×10^{-4}	4×10^{-4}

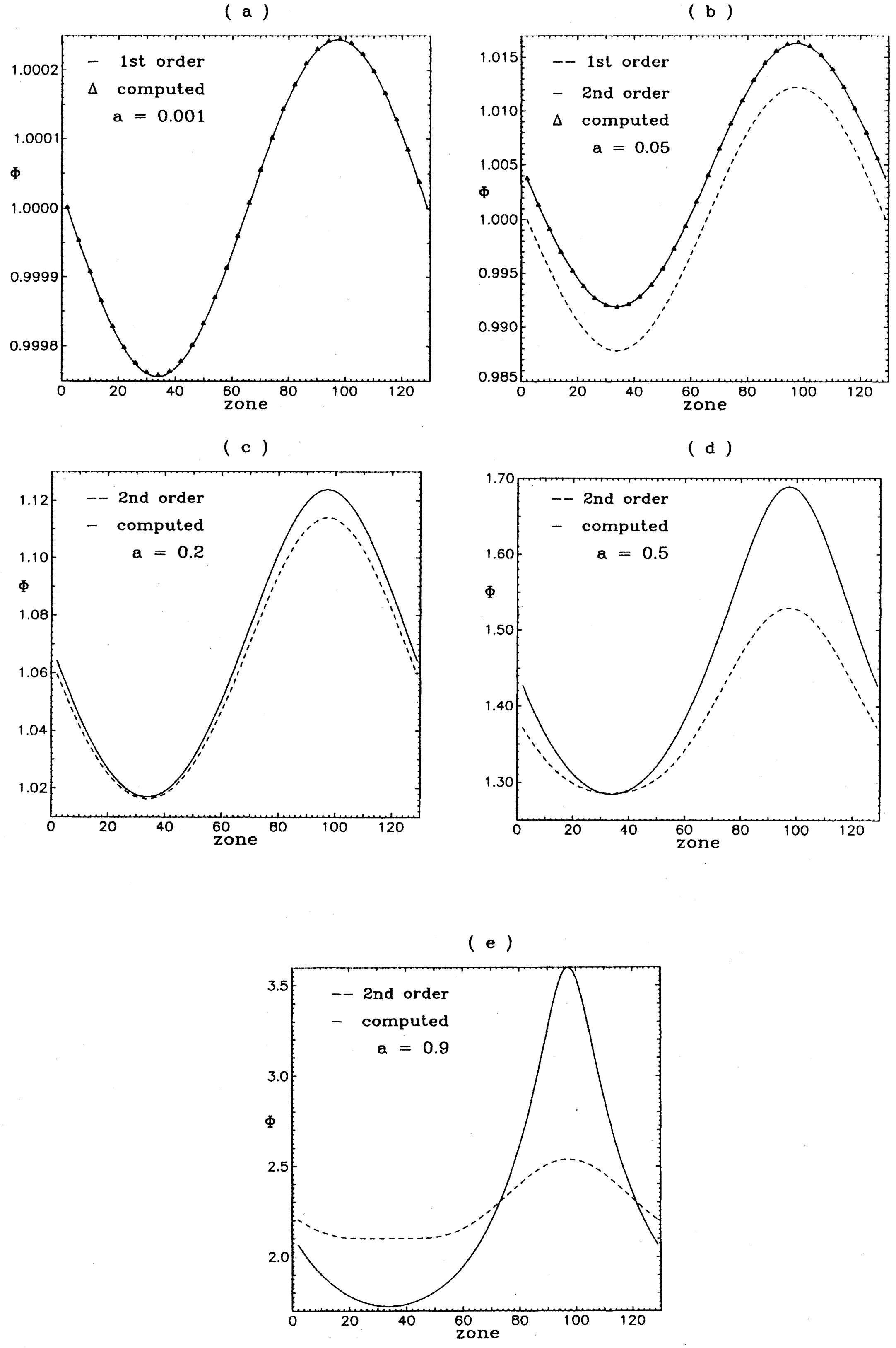

FIG. 3. Perturbative and code solutions for ϕ for the equal-amplitude–equal-wavelength case of Fig. 2. Note that there is no analytic solution for ϕ beyond the second order, Eqs. (4.16)–(4.18) in this case.

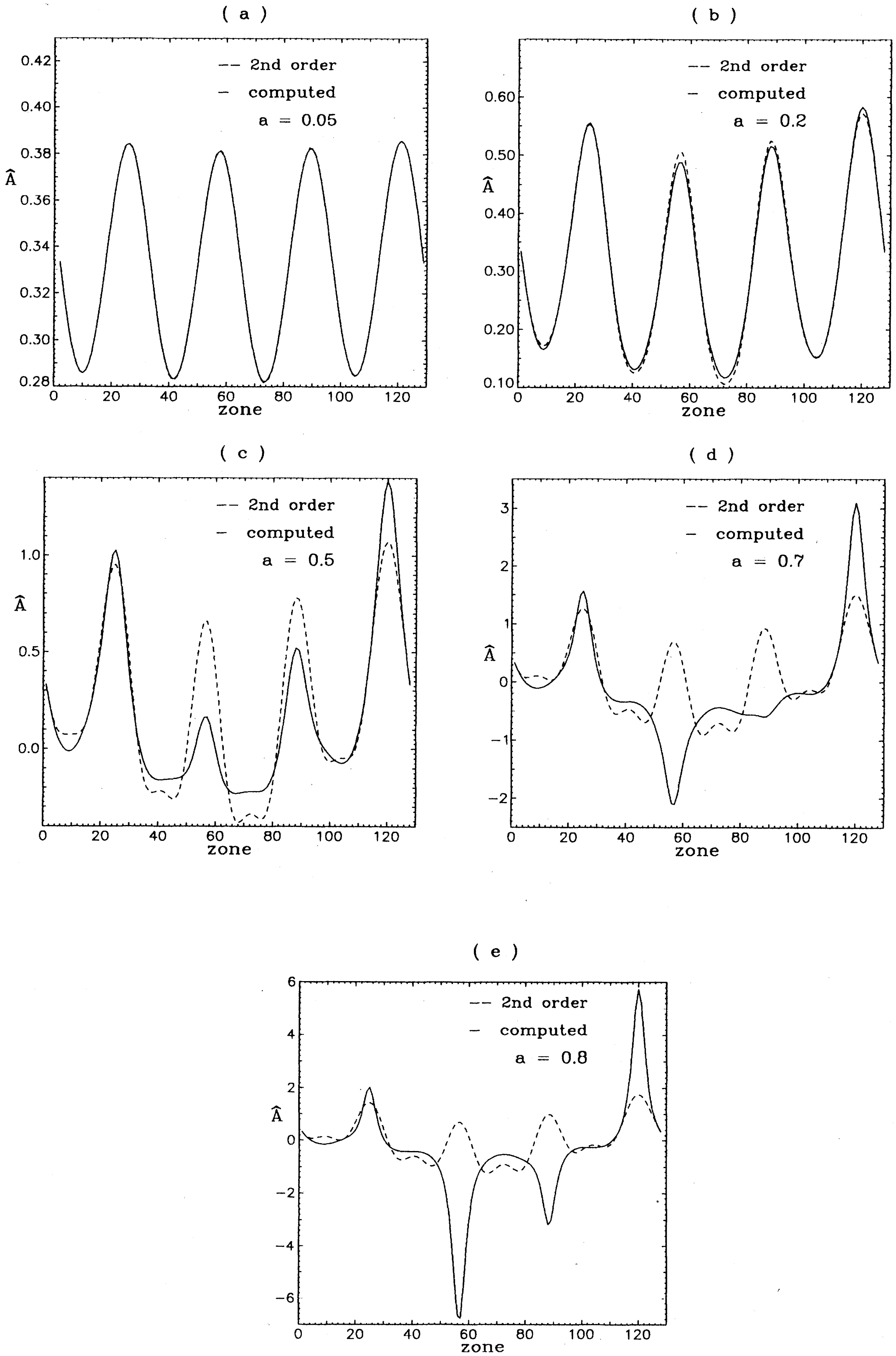

FIG. 4. Perturbative and code solutions for $\hat{A}$ for the case of free data with equal amplitudes but different wavelengths $4\lambda_h = 5\lambda_{\hat{\eta}} = L$. The numerical grid has 128 nodes.

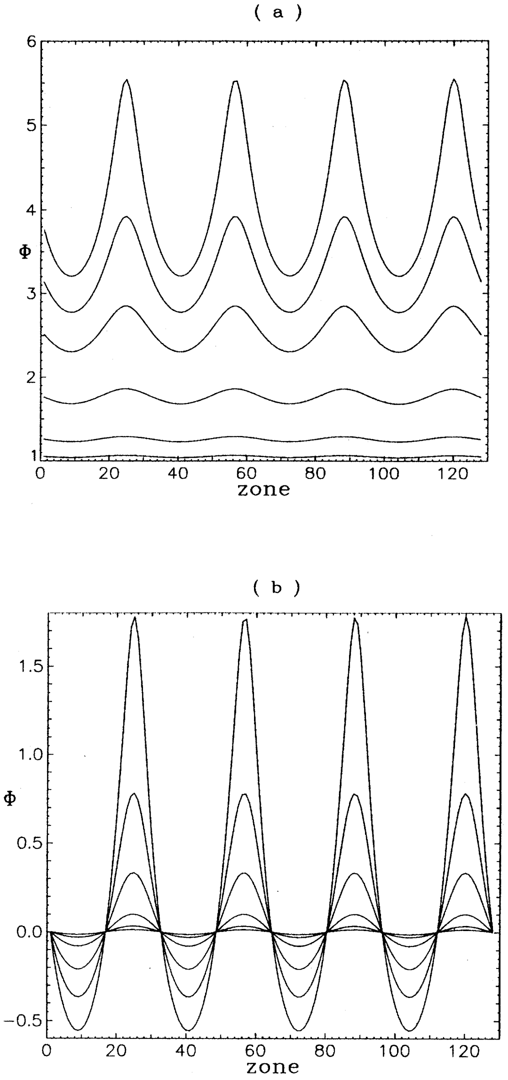

FIG. 5. Code solutions for ϕ for the cases of Fig. 4 on the actual scale in (a) and normalized so that $\phi_{z=0}=0$ in (b). The solutions increase in amplitude corresponding to the amplitudes of the perturbation in Figs. 4(a)–4(e).

TABLE IX. Error indicators for solving the Hamiltonian constraint for ϕ using 128 nodes. These results use the analytic solution given in Eqs. (5.19)–(5.22) with $\phi_0=10$, $h_0=1$, $\hat{A}_0=1$, tr$K=200$, and $m=1$.

Amplitude b of ϕ perturbation	$\mathrm{error}_{\mathrm{zone,abs}}$	$\mathrm{error}_{\mathrm{cum,rel}}$
0.01	8×10^{-12}	7×10^{-14}
0.1	8×10^{-11}	7×10^{-13}
1.0	8×10^{-10}	7×10^{-12}
5.0	4×10^{-9}	6×10^{-11}
8.0	1×10^{-7}	2×10^{-9}
9.0	2×10^{-6}	3×10^{-8}

TABLE X. Same as Table IX but for 16 nodes.

Amplitude b of ϕ perturbation	$\mathrm{error}_{\mathrm{zone,abs}}$	$\mathrm{error}_{\mathrm{cum,rel}}$
0.01	1×10^{-11}	1×10^{-12}
0.1	1×10^{-10}	1×10^{-11}
1.0	2×10^{-9}	1×10^{-10}
5.0	1×10^{-7}	4×10^{-9}
8.0	7×10^{-6}	2×10^{-7}
9.0	1×10^{-4}	2×10^{-6}

perturbation effectively lowers the resolution, leading to an increase in error. Comparing, for instance, Tables IX and X shows that the errors scale $\sim(\Delta z)^2$, although for smaller amplitudes the scaling diminishes. The $b=0.01$ case represents a $\sim10^{-12}$ relative term in the right-hand side of Eq. (5.22). The accuracy of solution indicated by Tables IX–XII represents ~1 part in 10^{12} of the desired solution. The saturation of error at small b is evidence for an insufficiently tight criterion for convergence in the Hamiltonian solution. We performed experiments in which the Hamiltonian convergence was relaxed to ~1 part in 10^{10}. In that case, the error residuals saturated at values $\sim10^2$ larger than those given in Tables IX–XII and were essentially identical between 16 and 128 zone calculations for $|b|\lesssim1$.

VI. SOME PARAMETER-SPACE RUNS

In this section we present some results of varying the amplitudes and wavelengths of the free data for the case of standing waves with a flat-space "background." Further examples of initial data sets, including traveling pulses localized in z on both cosmological and flat "backgrounds," are given in Ref. 31.

The first case we consider has free data in the form (4.12) with equal amplitudes $a=b$ and wavelengths $\lambda_h=\lambda_{\hat{\eta}}=L$. The results of varying the amplitude through the values $a=0.001$, 0.05, 0.2, 0.5, and 0.9 and solving the momentum constraint for $\hat{A}$ using 128 nodes are shown in Figs. 2(a)–2(e). The linear regime is shown in Fig. 2(a), where the code results match the first-order solution. Figure 2(b) shows the second-order regime in which the code results match the second-order solution, and both of these deviate from the first-order solution. The nonlinear effects continue to build in Figs. 2(c)–2(e), which show the code and exact analytic solutions deviating more and more from the second-order case. The re-

TABLE XI. Same as Table IX but for the case $m=3$.

Amplitude b of ϕ perturbation	$\mathrm{error}_{\mathrm{zone,abs}}$	$\mathrm{error}_{\mathrm{cum,rel}}$
0.01	2×10^{-11}	1×10^{-12}
0.1	2×10^{-10}	1×10^{-11}
1.0	2×10^{-9}	1×10^{-10}
5.0	1×10^{-7}	4×10^{-9}
8.0	8×10^{-6}	2×10^{-7}
9.0	2×10^{-4}	4×10^{-6}

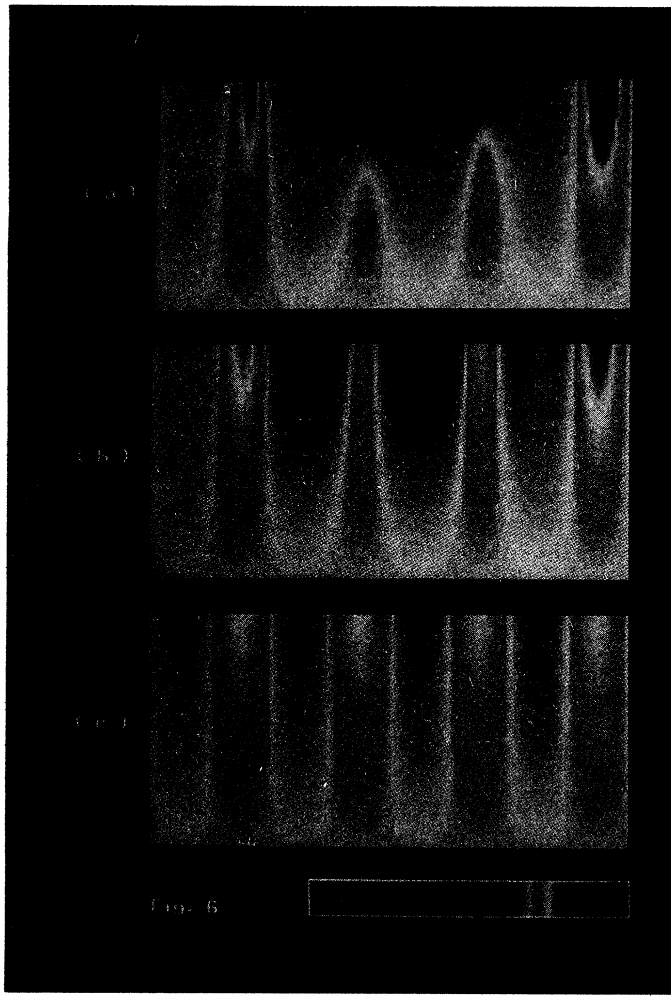

FIG. 6. $\hat{A}(z)$ is shown for equally spaced values of a in the range [0.001,0.8] (vertical axis) on a grid with 128 nodes (horizontal axis). (a) solves the full nonperturbative problem, (b) solves the second order, and (c) solves the linearized problem. For a fuller discussion see Sec. VI.

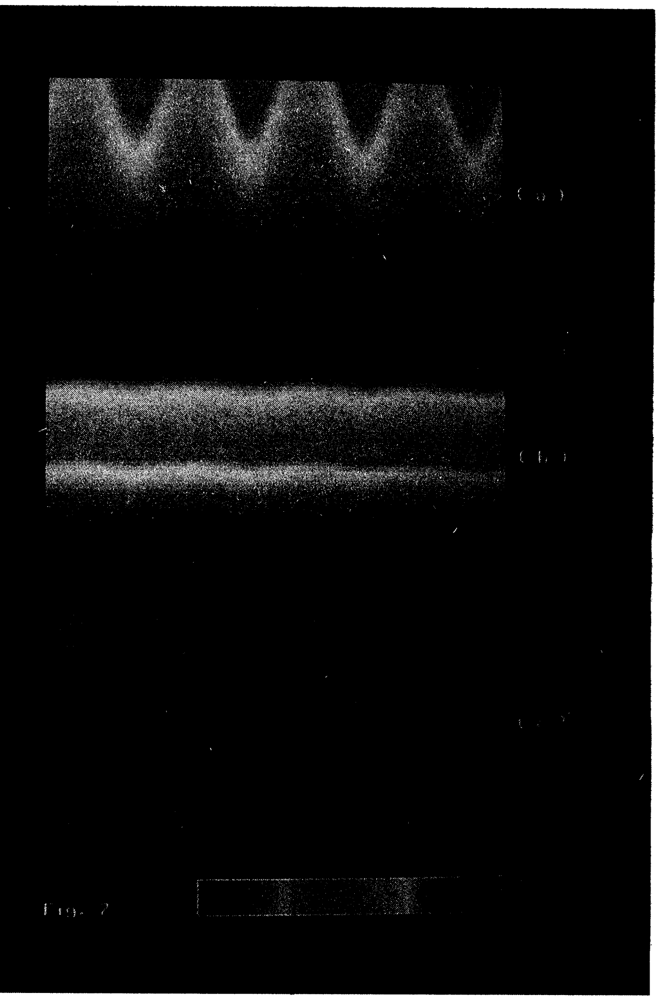

FIG. 7. Same as Fig. 6 but for ϕ. The full nonperturbative solution is shown in (a), the second-order solution in (b), and the linear in (c). See Sec. VI.

sults of solving the Hamiltonian constraint for ϕ are shown in Figs. 3(a)–3(e). Again, the first- and second-order regimes are shown in Figs. 3(a) and 3(b), respectively. Beyond second-order there is no analytic solution for ϕ, and so only the code and second-order results are plotted in Figs. 3(c)–3(e).

The momentum variable $\hat{A}$ shows a distinct trend toward building up a sharp asymmetric profile. That this is a strong nonlinear effect can be seen from the deviation of the solution from the second-order expression. Such a result may seem surprising at first, since the momentum constraint (2.14) is linear in $\hat{A}$. However, this equation is nonlinear in its source through the free data h. The dramatic change in shape of $\hat{A}$ as the amplitude of h increases is thus a response to nonlinearity in the source. The conformal factor ϕ also shows a trend toward an asymmetric peaked profile, although it remains much less distorted than $\hat{A}$. This behavior is due to the fact that the Hamiltonian constraint (2.15), while highly nonlinear in ϕ itself, is basically a Poisson-like equation. Such equations tend to produce relatively smooth responses to sharp sources, as is the case with potential due to a δ-function source such as a point charge. Note that the level of ϕ, given by $\phi_2=\phi_{km}$, increases with the amplitude of the free data. The level of $\hat{A}$ is constrained to remain constant by our boundary condition choice that $\hat{A}_{z=0}$ be

TABLE XII. Same as Table XI but for 16 nodes.

Amplitude b of ϕ perturbation	$\text{error}_{\text{zone,abs}}$	$\text{error}_{\text{cum,rel}}$
0.01	1×10^{-9}	8×10^{-11}
0.1	1×10^{-8}	8×10^{-10}
1.0	2×10^{-7}	9×10^{-9}
5.0	7×10^{-6}	3×10^{-7}
8.0	3×10^{-4}	1×10^{-5}
9.0	2×10^{-3}	9×10^{-5}

equal to the background value of $\hat{A}$ for all choices of the free data.

We also consider the case in which the free data have equal amplitudes but different wavelengths $4\lambda_h = 5\lambda_{\hat{\eta}} = L$. The results of solving for $\hat{A}$ are shown in Figs. 4(a)–4(e), where the amplitude of the free data takes the values $a = 0.05$, 0.2, 0.5, 0.7, and 0.8. Here, only the second-order and code solutions are shown. The full analytic solution for $\hat{A}$, while obtainable in principle, is very unwieldy in this case. Since we have already tested the code extensively (see Sec. V), we are confident in considering only the numerical solution here. Code solutions for ϕ are shown in Fig. 5(a) on the actual scale and in Fig. 5(b) normalized so that $\phi_{z=0} = 0$.

Note that the solutions are dominated by the $4\lambda = L$ signal in h; this is expected from the momentum constraint (2.14b) in which we see that the behavior of h dominates the source. For large values of a some of the peaks actually turn over and become valleys. Higher modes also become visible as the nonlinear effects increase. The curves for ϕ again are smoother. They increase in overall amplitude, steepness, and level as the amplitude of the free data increases.

The results of these parameter space runs are shown as color images in Figs. 6 and 7. Each separate image is made up of 50 separate, 128-node runs with a varying in the range [0.001,0.8] at equally spaced values. The z axis runs along the horizontal (long) direction of each image and a increases upward along the vertical (short) direction. Figure 6 shows the value of $\hat{A}$ in colors ranging from purple (low value) to red (high value); all three images in Fig. 6 are on the same color scale, given by the color bar at the bottom of the figure. Figure 7 does the same for ϕ. The color maps were chosen carefully to bring out as much information in the images as possible. In both Figs. 6 and 7 the top image (a) gives the results of solving the full nonperturbed equation, (b) gives the results of solving the equations to second order, and (c) gives the results of solving to first order.

These images provide a wealth of information about the solutions to the momentum and Hamiltonian constraints and a good means of assessing the effects of nonlinearity. For example, the bottom part of each panel in Figs. 6 and 7 is the same (first-order regime) while the middle parts of (a) and (b) are the same (second-order regime). The upper portions differ considerably, since this is where the nonlinear effects are the strongest. The clear symmetry of the sinusoidal oscillations in $\hat{A}$ in the first-order solutions [Fig. 6(c)] gives way to differences in shape and strength among the peaks in the second-order regime [cf. Figs. 4(a) and 4(b) with Fig. 6(b)]. The full nonperturbative solution for $\hat{A}$ shows qualitatively different behavior [Figs. 4(c)–4(e) and Fig. 6(a)]. Similarly, the sinusoidal oscillations in ϕ about a fixed level at first order [Fig. 7(c)] develop a rise in level at second order [Fig. 7(b)] and distinctly asymmetrical profiles in the nonperturbative regime [Fig. 5 and Fig. 7(a)]. Figure 7 shows the rise in level of the second-order solution, which outstrips that of the nonperturbative solution for large values of a. Direct visual comparison of the images in Figs. 6 and 7 clearly demonstrates the differences in solutions to the initial-value equations in the perturbative and full nonlinear regimes.

ACKNOWLEDGMENTS

We are pleased to acknowledge stimulating discussions with C. Evans and J. W. York. We also thank D. Cox for providing us with a copy of her interactive graphics editor ICARE, which was used to generate the images in Figs. 6 and 7. Computations reported here were carried out at the National Center for Super Computer Applications (University of Illinois). This work was supported by NSF Grants Nos. PHY-8404931, PHY-8417918, PHY-8451732, PHY-8706315, and PHY-8806567, and by Cray Research, Inc.

---

[1] L. L. Smarr, in *Sources of Gravitational Radiation,* edited by L. L. Smarr (Cambridge University Press, Cambridge, England, 1979), p. 245.

[2] D. M. Eardley, in *Dynamical Spacetimes and Numerical Relativity,* edited by J. M. Centrella (Cambridge University Press, Cambridge, England, 1986), p. 347.

[3] C. R. Evans, in *Dynamical Spacetimes and Numerical Relativity,* edited by J. M. Centrella (Cambridge University Press, Cambridge, England, 1986), p. 3.

[4] T. Piran and R. F. Stark, in *Dynamical Spacetimes and Numerical Relativity,* edited by J. M. Centrella (Cambridge University Press, Cambridge, England, 1986), p. 40.

[5] V. Belinski and V. Zakharov, Zh. Eksp. Teor. Fiz. **75**, 1955 (1978) [Sov. Phys. JETP **48**, 985 (1978)].

[6] V. Belinski and V. Zakharov, Zh. Eksp. Teor. Fiz. **77**, 3 (1979) [Sov. Phys. JETP **50**, 1 (1979)].

[7] R. Jantzen, Nuovo Cimento **59B**, 287 (1980).

[8] B. Carr and E. Verdaguer, Phys. Rev. D **28**, 2995 (1983).

[9] J. Ibañez and E. Verdaguer, Phys. Rev. Lett. **51**, 1313 (1983).

[10] J. Ibañez and E. Verdaguer, Phys. Rev. D **31**, 251 (1985).

[11] M. Norman and K.-H. Winkler, in *Astrophysical Radiation Hydrodynamics,* edited by K.-H. Winkler and M. Norman (Reidel, Dordrecht, 1986), pp. 187 and 223.

[12] N. Zabusky, J. Comput. Phys. **43**, 195 (1981).

[13] N. Zabusky, Phys. Today **37**, No. 7, 36 (1984).

[14] J. Centrella, in *Dynamical Spacetimes and Numerical Relativity,* edited by J. Centrella (Cambridge University Press, Cambridge, 1986), p. 123.

[15] R. Arnowitt, S. Deser, and C. W. Misner, in *Gravitation: An Introduction to Current Research,* edited by L. Witten (Wiley, New York, 1962), p. 227.

[16] J. W. York, in *Sources of Gravitational Radiation,* edited by L. L. Smarr (Cambridge University Press, Cambridge, England, 1979), p. 83.

[17] R. Gowdy, Phys. Rev. Lett. **27**, 826 (1971).

[18] B. Berger, Ann. Phys. (N.Y.) **83**, 458 (1974).

[19] J. Centrella and J. R. Wilson, Astrophys. J. **273**, 428 (1983).

[20] J. Centrella and J. R. Wilson, Astrophys. J. Suppl. **54**, 229 (1984).

[21] J. Centrella, R. Matzner, T. Rothman, and J. Wilson, Nucl. Phys. **B266**, 171 (1986).

[22] H. Kurki-Suonio, J. Centrella, R. Matzner, and J. Wilson,

Phys. Rev. Rev. D **35**, 435 (1987).

[23] Y. Choquet-Bruhat, in *Abstracts of Contributed Papers, 8th International Conference on General Relativity and Gravitation* (University of Waterloo, Ontario, 1977).

[24] D. Brill, in *Spacetime and Geometry,* edited by R. A. Matzner and L. C. Shepley (University of Texas Press, Austin, 1982).

[25] E. Kasner, Am. J. Math. **43**, 217 (1921).

[26] I. S. Gradshteyn and I. M. Rhyzik, *Table of Integrals, Series, and Products* (Academic, New York, 1980).

[27] R. W. Hornbeck, *Numerical Methods* (Prentice-Hall, Englewood Cliffs, N.J., 1975).

[28] N. O'Murchadha and J. W. York, J. Math. Phys. **14**, 1551 (1973).

[29] D. S. Kershaw, J. Comput. Phys. **26**, 43 (1978).

[30] C. R. Evans, (private communication).

[31] P. Anninos, J. Centrella, and R. Matzner, in *Frontiers of Numerical Relativity,* edited by C. Evans, L. S. Finn, and D. Hobill (Cambridge University Press, Cambridge, England, in press).

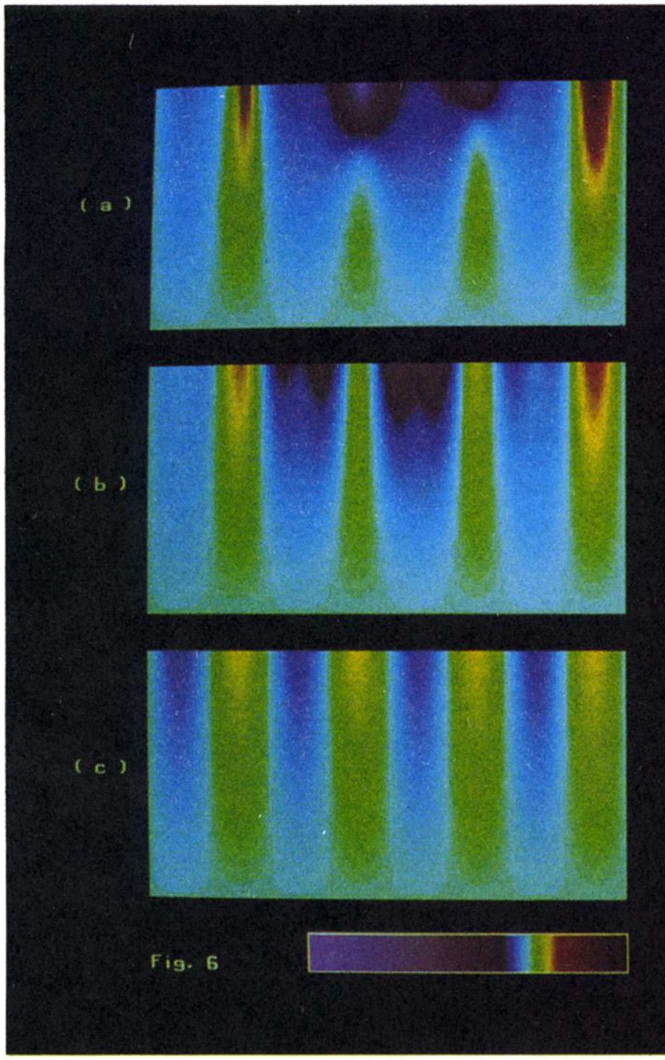

FIG. 6. $\hat{A}(z)$ is shown for equally spaced values of a in the range [0.001,0.8] (vertical axis) on a grid with 128 nodes (horizontal axis). (a) solves the full nonperturbative problem, (b) solves the second order, and (c) solves the linearized problem. For a fuller discussion see Sec. VI.

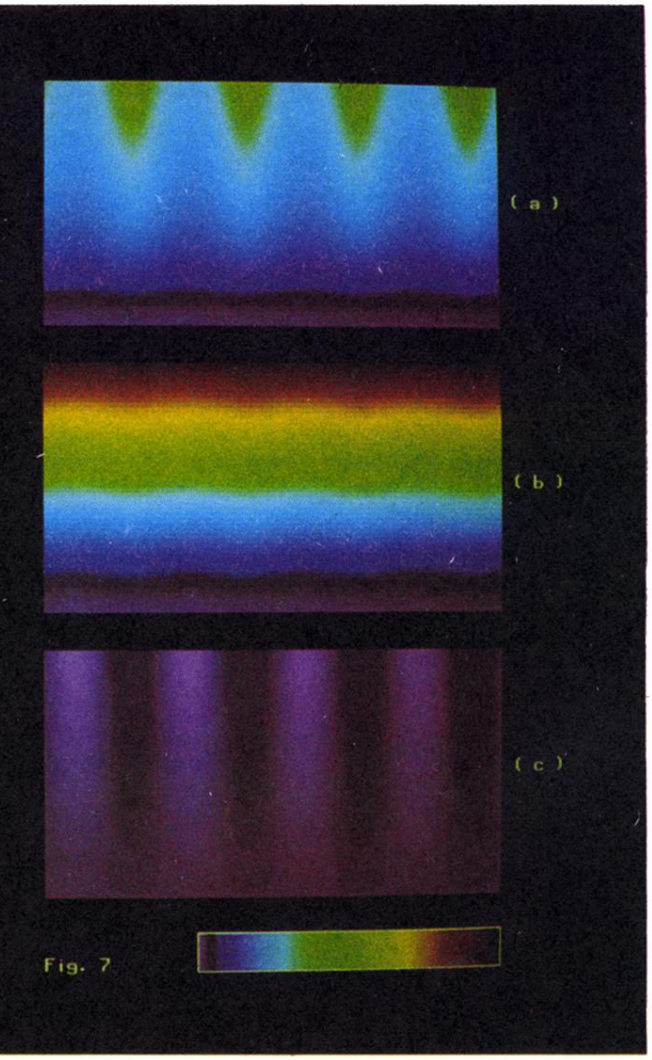

FIG. 7. Same as Fig. 6 but for ϕ. The full nonperturbative solution is shown in (a), the second-order solution in (b), and the linear in (c). See Sec. VI.